

Accurate determination of the optical performances of antireflective coatings by low coherence reflectometry

Michel Lequime^{1,*} and Julien Lumeau²

¹Institut Fresnel, UMR CNRS 6133, Université Paul Cézanne—Ecole Centrale Marseille—Université de Provence, Domaine Universitaire de Saint-Jérôme, 13397 Marseille Cedex 20, France

²College of Optics and Photonics, CREOL, University of Central Florida, P.O. Box 162700, Orlando, Florida 32816-2700, USA

*Corresponding author: michel.lequime@fresnel.fr

Received 6 February 2007; revised 27 April 2007; accepted 22 May 2007;
posted 22 May 2007 (Doc. ID 79791); published 8 August 2007

We propose to use optical low coherence reflectometry to measure the reflectance of both faces of a plane substrate with one side coated in antireflective layers. We identify, through a detailed theoretical analysis, the optimum configuration and evaluate the expected sensitivity and accuracy of some realistic examples. Finally, we experimentally demonstrate the ability of this method to quantify reflection coefficients as low as 5×10^{-7} . That way, an accurate characterization of the performances, at 1550 nm, of antireflective coatings deposited on various plane substrates is achieved. © 2007 Optical Society of America

OCIS codes: 120.3180, 120.5700, 310.1210, 310.6860.

1. Introduction

The accurate measurement of the residual reflectance of substrates coated with antireflective coatings remains today a key point for the development of optical systems with optimized performances. When the two faces of an optical window are coated with the same stack of dielectric thin films, a simple measurement of the global reflectance of this component can be used without a problem to evaluate the mean performances of the coatings deposited on each face. The same kind of approach can also be used for a single-side coated component when the residual reflectance of the coated surface keeps the same order of magnitude as the uncoated one (ratio smaller than 10, for instance). But when this antireflective coating is very efficient and deposited on only one face of the substrate (for instance, the front face), it becomes difficult to extract an accurate value of this reflectance from global reflection or transmission measurements.

To eliminate the unwanted contribution of the rear face of this plane window, many experimental schemes can be imagined. The first one is based on

the use of confocal detection, and requires focusing the measurement beam on the coated surface with a high numerical aperture objective. Such a method induces an averaging of the performances of the stack on a large range of angles of incidence and accordingly leads to poor quality measurements, especially for all the designs whose efficiency is characterized by a strong angular dependence. The second scheme uses the same concept of spatial filtering, but this time on small section collimated light beams: it is based on the appearance of a lateral shift of the beam reflected by the rear face of the window for nonzero angles of incidence and on the use of a stop to eliminate the unwanted reflection. We stress that this lateral displacement is proportional to the thickness t of the window and remains smaller than $t/2$ for any angles of incidence, the maximum being reached around 45° . It means that the use of this method is restricted to quite thick windows with coatings optimized for nonzero incidences. In the case of thin windows and zero angles of incidence, the only remaining solutions are associated with a modification of the optical properties of this rear face, either by grounding the surface or by using an immersion liquid. In some applications, these very invasive methods can-

not be implemented and this justifies why we propose to use optical low-coherence reflectometry (OLCR).

OLCR is a powerful method for interferometric detection and ranging, widely used for many years in many applications, such as optical fiber sensors and sensing networks [1–4], optical waveguide characterization [5,6], noninvasive imaging of retina or biological tissues with micrometer scale spatial resolution [7–9], or fine characterization of optical elements [10–12]. Basically, this method uses a broadband source (instead of a narrowband one such as a laser) to illuminate an interferometric device to restrict the useful interference signal around the zero optical path difference (OPD). In this manner the contributions of some specific interfaces separated by an optical path length larger than the coherence length of the source can be identified. However, this multiplexing ability, especially used in fiber optic sensing networks, does not hide another great advantage of OLCR, i.e., its sensitivity, which is naturally provided by the coherent nature of the detection scheme.

In Section 2 we provide a brief description of a standard OLCR setup. Section 3 is devoted to a detailed theoretical analysis of the method: first it includes a study of the effect of the fiber coupling efficiency changes, then an analysis of the influence of the dispersion phenomena, and finally an evaluation of the consequences of the spectral averaging on the accuracy of the results. Experimental results obtained with an OLCR setup on bare and coated substrates are given in Section 4. Section 5 summarizes the main results and describes some possible improvements.

2. Description of the OLCR Setup

Let us consider the basic configuration of an OLCR as described in Fig. 1. The light provided by a broadband source is directly launched into port 1 of a 3 dB single mode coupler used as the beam splitter of a guided Michelson interferometer. The extremity of one of the output fibers of this coupler (for instance port 2) is located near the object focal plane of a collimating lens to produce a diffraction limited Gaussian beam, which is backreflected by the plane sample under test (thickness t , refractive index n). This sample's backreflected power includes several terms, i.e., the reflection on the front face, the reflection on the rear face, and the additional echoes created by the multiple reflections inside the window. The light delivered by the third port of this fiber coupler is collimated by a second objective and backreflected by a metallic plane mirror mobile along the z axis. All these backreflected optical beams are then mixed into the same

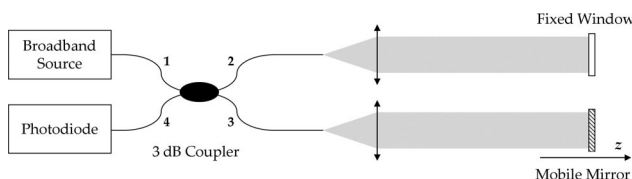


Fig. 1. Schematic description of an OLCR.

3 dB coupler, and the resulting interference signal is recorded by a photodiode connected to the fourth port of this device.

At the detector level, the complex amplitude of the light beam backreflected by the plane mirror is given by

$$A_M(\sigma) = A(\sigma) \sqrt{L^2 Y (1 - Y)} \sqrt{R_M \eta_M(z)} \times e^{4i\pi\sigma(z+f)} e^{i\varphi_M}, \quad (1)$$

where $A(\sigma)$ is the amplitude of the source at wave-number σ , Y is the branching ratio of the coupler, L is its excess loss level, R_M is the reflection coefficient of the metallic mirror, $\eta_M(z)$ is the efficiency of the coupling in the single mode fiber of the light backreflected by this mirror at a distance z from the collimating lens, f is the focal length of this lens, and φ_M is the phase variation of the light beam at the reflection on the metallic mirror.

In the same way, the amplitude of the light beam backreflected by the plane sample is given by

$$A_S(\sigma) = A(\sigma) \sqrt{L^2 Y (1 - Y)} \sum_{k=1}^{\infty} \sqrt{R_k \eta_k} \times e^{4i\pi\sigma(z_k+f)} e^{i\varphi_k}, \quad (2)$$

where R_k is the reflection coefficient corresponding to the k -order echo on the sample, η_k is the efficiency of the backcoupling in the single mode fiber associated with this echo, φ_k is the corresponding phase variation, z_1 is the distance between the collimating lens and the front face of the sample, and z_k are some specific distances associated with the path of the light beam inside the sample and defined by $z_k = z_1 + (k - 1)nt$.

The optical power $P_D(\sigma)$ resulting from the interference between these two light beams is then given by

$$P_D(\sigma) = |A_M(\sigma) + A_S(\sigma)|^2 = P(\sigma) L^2 Y (1 - Y) \times [C_S + C_M(z) + C_0(z)], \quad (3)$$

where C_S , $C_M(z)$, and $C_0(z)$ are three terms, respectively, connected with sample–sample correlations, sample–mirror correlations, and a dc level, i.e.,

$$C_S = 2 \sum_{k=1}^{\infty} \sqrt{R_k \eta_k} \times \sum_{l=k+1}^{\infty} \sqrt{R_l \eta_l} \cos[4\pi\sigma(z_k - z_l) + (\varphi_k - \varphi_l)], \quad (4)$$

$$C_M(z) = 2 \sqrt{R_M \eta_M(z)} \times \sum_{k=1}^{\infty} \sqrt{R_k \eta_k} \cos[4\pi\sigma(z - z_k) + (\varphi_M - \varphi_k)], \quad (5)$$

$$C_0(z) = R_M \eta_M(z) + \sum_{k=1}^{\infty} R_k \eta_k. \quad (6)$$

The electric current I delivered by the photodiode is given by the integration of the relation in Eq. (3) over all the wavenumbers:

$$I(z) = \int_{\sigma} S(\sigma)P_D(\sigma)d\sigma, \quad (7)$$

where S corresponds to the sensitivity of the detector.

Let us suppose now that the spectral profile of the source can be described by a Gaussian function, i.e.,

$$P(\sigma) = \frac{P_0}{\delta\sigma\sqrt{\pi}} e^{-\left[\frac{\sigma-\sigma_0}{\delta\sigma}\right]^2}, \quad (8)$$

where P_0 is the total light power emitted by the broadband source, σ_0 is its central wavenumber, and $\delta\sigma$ is its spectral width. Let us suppose also that the optical thickness nt of the window under test is sufficient to ensure a lack of interference between the different echoes, which means that

$$nt \pi \delta\sigma = nt \pi \frac{\Delta\lambda}{\lambda_0^2} \gg 1. \quad (9)$$

Finally, let us suppose we can neglect the spectral dependence of the sensitivity of the photodiode as well as the dispersion effects introduced by the wavelength dependence of the refractive index of the window and the reflection coefficients of the structure. By using such assumptions, we can compute the expression of the electric current in the function of mirror position z :

$$\begin{aligned} I(z) = & SP_0Y(1-Y)L^2 \left\{ C_0(z) + 2\sqrt{R_M\eta_M(z)} \right. \\ & \times \sum_{k=1}^{\infty} \sqrt{R_k\eta_k} e^{-[2\pi\delta\sigma(z-z_k)]^2} \cos[4\pi\sigma_0(z-z_k) \\ & \left. + (\varphi_M - \varphi_k)] \right\}. \end{aligned} \quad (10)$$

Moreover, if the metallic mirror is translated at a constant speed v , an intermediate frequency F ($F = 2v\sigma_0$) is generated in the interferometric response of the reflectometer and can be used to perform, around this frequency, a filtering of the time signal $I(t)$ delivered by the photodiode. The resulting filtered signal $I_F(z)$ is finally given by

$$\begin{aligned} I_F(z) = & 2SP_0Y(1-Y)L^2 \sqrt{R_M\eta_M(z)} \\ & \times \sum_{k=1}^{\infty} \sqrt{R_k\eta_k} e^{-[2\pi\delta\sigma(z-z_k)]^2}. \end{aligned} \quad (11)$$

Figure 2 shows the theoretical shape of this filtered signal $I_F(z)$ when the sample under test is a 1 mm thick uncoated silica window and when the broadband source has a 1530 nm central wavelength and a 5 nm half-width at $1/e$.

The first echo corresponds to the reflection on the front face of the silica plate [$R_1 = R$; $z = z_1$], the second one to the reflection on the rear face [$R_2 = (1 - R)^2R$; $z = z_2 = z_1 + nt$], while the third one is associated with the first multiple reflection in

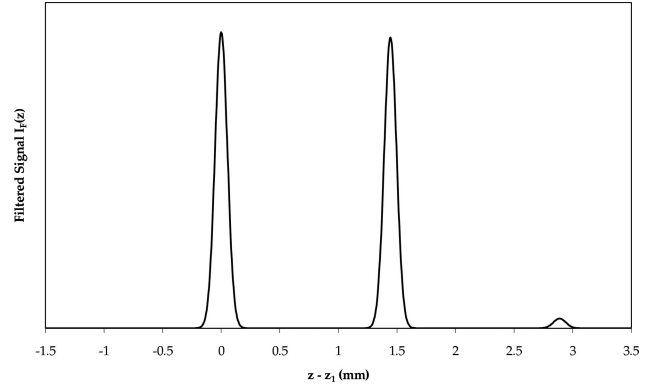


Fig. 2. Filtered signal recorded with an uncoated 1 mm thick silica window.

the window, including a reflection on the rear face, an internal reflection on the front face, and a new reflection on the rear face [$R_3 = (1 - R)^2R^3$; $z = z_3 = z_1 + 2nt$].

A simple way to overcome most of the calibration problems that can occur with such an OLCR device is to place the uncoated face of the window in front and to use the intensity of the first echo S_1 as a reference signal with respect to which the intensities of all the following echoes S_k will be renormalized. By using such a strategy, the result of the measurement becomes

$$M_k = \frac{S_k}{S_1} = \sqrt{\frac{R_k}{R_1}} \times \sqrt{\frac{\eta_k\eta_M(z_k)}{\eta_1\eta_M(z_1)}}, \quad (12)$$

and, as a consequence, the reflectance coefficient R_2 on the coated rear face can be extracted by applying the following relation:

$$R_2 = \left(\frac{n-1}{n+1}\right)^2 \frac{\eta_1\eta_M(z_1)}{\eta_2\eta_M(z_2)} \times \left[\frac{S_2}{S_1}\right]^2. \quad (13)$$

The accuracy of our determination is then driven by the effective values of the backcoupling efficiencies η . It is one of the reasons (but not the only one) for which a detailed theoretical analysis of the implementation of an OLCR setup for the measurement of the optical performances of antireflective coatings is required.

3. Theoretical Analysis

A. Backcoupling Efficiencies

For computing the backcoupling efficiencies in the core of the single mode fiber, we shall use the Gaussian beam propagation formalism [13]. Let us call w_0 the mode radius of the fiber, w_1 is the waist of the beam backreflected by a plane interface located at a distance z of the collimating lens, and g is the axial gap between the position of this waist and the fiber core. Then the backcoupling efficiency η is given by

the following relation [14,15]:

$$\eta = \frac{4w_1^2 w_0^2}{(w_1^2 + w_0^2)^2 + (\lambda_0 g / \pi)^2}. \quad (14)$$

Let us consider first the case of the plane mirror and let us suppose that the distance d_M between the fiber extremity and the collimating lens is chosen to ensure that the distance between the image waist and the lens be equal to z_1 . When the plane mirror is located at this specific position, the position of the waist after reflection is the same as before reflection and the last image through the lens is by symmetry superimposed on the fiber extremity. Then $w_1 = w_0$, $g = 0$, and at the end $\eta_M(z_1) = 1$. When the mirror is located at a position z different from z_1 , the waist of the beam after reflection is located at a position that is symmetric to one before reflection with respect to the mirror. Hence Gaussian beam propagation formalism [13] has to be used for computing the final position of the waist after the lens. These computations are not really complicated but have to be performed with care. A better way to quickly obtain the final relations is to choose the intermediate space (i.e., the one where the mirror is located) for rewriting the coupling efficiency relationship in Eq. (14) under the alternative form

$$\eta_M(z) = \frac{4W_1^2 W_0^2}{(W_1^2 + W_0^2)^2 + \left[\frac{2\lambda_0(z - z_1)}{\pi} \right]^2}, \quad (15)$$

where W_0 (respectively, W_1) is the waist radius associated to the image of the fiber extremity through the lens (respectively, through the lens and the mirror). The use of the Gaussian beam relationships leads easily to

$$W_1 = W_0 = \frac{\lambda_0 f}{\pi w_0}, \quad (16)$$

where f is the focal length of the lens, and then to the final expression for the backcoupling efficiencies in the case of the plane mirror:

$$\eta_M(z_k) = \frac{1}{1 + \left[\frac{\pi w_0^2 (z_k - z_1)}{\lambda_0 f^2} \right]^2} = \frac{1}{1 + \left[\frac{\pi w_0^2 (k - 1) n t}{\lambda_0 f^2} \right]^2}. \quad (17)$$

By using the same kind of approach, we are able to compute the coupling efficiencies of the beams backreflected by the plane window. We obtain in this case

$$\eta_k = \frac{1}{1 + \left[\frac{\pi w_0^2 (k - 1) t}{n \lambda_0 f^2} \right]^2}. \quad (18)$$

It is important to stress here a small difference in the behavior of the two arms of the interferometer with respect to the thickness of the window: the plane mirror arm involves the optical thickness of this window, i.e., the product $t \times n$, while the window arm involves its apparent thickness, i.e., the ratio t/n .

Let us suppose now that our OLCR setup is characterized by the following parameters: $\lambda_0 = 1530$ nm; $w_0 = 5.25$ μ m; $f = 25.3$ mm; $z_1 = 220$ mm; $t = 1$ mm; $n_0 = 1.444$. We can then compute the values of the corrective factors appearing in Eq. (13), i.e., η_1 , $\eta_M(z_1)$, η_2 , and $\eta_M(z_2)$, and all these terms are extremely close to one. It means that the accuracy of the measurement method is not decreased by the presence of these backcoupling efficiency terms.

However, this positive conclusion implicitly assumes that first the displacement of the mirror is performed without tilt (which is possible by selecting a high quality translation stage), but also that the two faces of the window are perfectly parallel, which is more difficult to ensure in many practical cases. Now, if the window has a small wedge (angle α), the backcoupling efficiency will be modified in accordance with the following relation [15]:

$$\eta(\alpha) = \eta(0) e^{-\left[\frac{2f\alpha}{w_0} \right]^2}, \quad (19)$$

which means that a 7 arc s wedge is sufficient to induce a 10% change in the η value. This constraint is thus very severe and shall be absolutely relaxed. A possible way to overcome this problem is to slightly change the position of the fiber extremity with respect to the lens in the sample arm, to form as before an image of the fiber waist on the front face of the window, but in a focused configuration (instead of a collimated one). This modification shall, however, ensure that the zero OPD between the two arms is achieved for the same z_1 position of the mirror. Figure 3 provides a schematic description of this alternative focused configuration.

In this alternative configuration, we can again establish the relationship describing the coupling efficiencies of the various beams backreflected by the plane window, i.e.,

$$\eta_k = \frac{1}{1 + \left[\frac{(k - 1) t \lambda f^2}{n \pi w_0^2 (z_E - f)^2} \right]^2}, \quad (20)$$

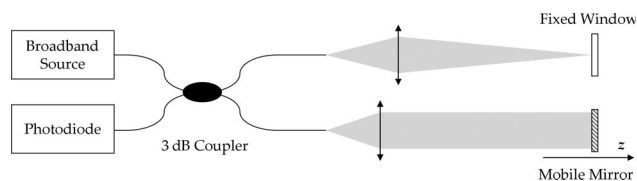


Fig. 3. OLCR, alternative focused configuration.

where z_E corresponds to the distance between the lens and the front face of the window and is defined here by

$$z_E = \frac{z_1 + f}{2} \left[1 + \sqrt{1 - \frac{4f}{z_1 + f}} \right]. \quad (21)$$

By using the same numerical data as before, we are able to compute the z_E distance ($z_E = 216.6$ mm), then the distance between the lens and the extremity of the fiber ($d_E = 28.7$ mm), and finally, the nominal values of the backcoupling efficiencies associated with the three first echoes, i.e., $\eta_1 = 100\%$; $\eta_2 = 95.6\%$; and $\eta_3 = 84.5\%$.

This slight decrease of efficiency with the echo order is the price to pay for reaching better tilt and wedge tolerances. Indeed, the degradation induced by a window wedge α now becomes

$$\eta(\alpha) = \eta(0) e^{-\left[\frac{2\pi\omega_0\alpha}{\lambda} \frac{z_E - f}{f} \right]^2}, \quad (22)$$

which leads to a wedge tolerance of several arc min, as expected. It is important to note here that the impact of this decreasing of the backcoupling efficiencies remains nevertheless moderate, around 5% in relative value.

The use of a focused configuration in the mirror arm also can be envisaged, but it has in fact negative impacts on the accuracy of the final result. Identical conclusions are obtained if we replace the moving of the mirror by a translation of the window, and this last conclusion is because of the behavior difference of the two arms with respect to the t and n terms previously stressed. Hence, the only efficient solution is to locate the image waist inside the window in the alternative configuration corresponding to Fig. 3, to well balance the efficiency of the two first reflections. This open loop approach is not really required here because of the small values of the corrective factors.

Finally, all this analysis shows that the best solution for our measurement will be to use the configuration in which the reference beam reflected by the mobile mirror is collimated while the measure beam is focused on the front face of the window.

B. Window Refractive Index Dispersion Effects

If we now take into account the wavelength dependence of the refractive index of the window, Eq. (11) becomes [16]

$$I_F(z) = 2SP_0 Y (1 - Y) A^2 \sqrt{R_M} \eta_M(z) \sum_{k=1}^{\infty} \sqrt{R_k} \eta_k G_k(z), \quad (23)$$

with

$$G_k(z) = \sqrt{1 + \theta_k^2} e^{-\left[2\pi \frac{\delta\sigma}{\sqrt{1 + \theta_k^2}} (z - z_k - \delta z_k) \right]^2}, \quad (24)$$

$$\theta_k = 2\pi(k - 1)t\lambda_0 \times \left(\frac{\delta\lambda}{\lambda_0} \right)^2 \times \left(\frac{\partial^2 n}{\partial \lambda^2} \right)_{\lambda_0}, \quad (25)$$

$$\delta z_k = -(k - 1)t\lambda_0 \times \left(\frac{\partial n}{\partial \lambda} \right)_{\lambda_0}, \quad (26)$$

where λ_0 is the central wavelength of the source and $\delta\lambda$ its spectral half-width at $1/e$. This spectral dependence obviously has no effect on the reflection on the front face of the window, but for the other echoes ($k \geq 2$) this dispersion introduces three main changes, i.e., a displacement of the position of the echo ($z_k \rightarrow z_k + \delta z_k$), a broadening of this echo ($\Delta z_k \rightarrow \Delta z_k \cdot \sqrt{1 + \theta_k^2}$), and a decrease in this maximum intensity ($I_k \rightarrow I_k / \sqrt{1 + \theta_k^2}$).

The first two changes are really troubling only if the physical separation between the various echoes is no longer ensured. The last effect can have more direct impact on the accuracy of the method. To quantify the impact of these refractive index dispersion phenomena, we have chosen to evaluate their effects on two representative examples, i.e., a 1 mm thick silica window and a 350 μm thick InP wafer. First, the wavelength dependence of the refractive index is defined for silica by [17]

$$n^2(\lambda) = 1 + \lambda^2 \left[\frac{0.6961663}{\lambda^2 - (0.0684043)^2} + \frac{0.4079426}{\lambda^2 - (0.1162414)^2} + \frac{0.8974794}{\lambda^2 - (9.896161)^2} \right], \quad (27)$$

where λ is in micrometers, and then for InP by [18]

$$n^2(\lambda) = 7.283 + \frac{2.337\lambda^2}{\lambda^2 - 0.387 \cdot 10^6}, \quad (28)$$

where λ is this time in nanometers. In Table 1 we have summarized the numerical values of the parameters involved in the description of these window dispersion effects for a light source centered at 1530 nm and having a spectral half-width of 5 nm at $1/e$.

The refractive index dispersion of the selected windows does not induce any kind of overlapping of the echoes, and the broadening of the backecho is too low

Table 1. Window Dispersion Phenomena—Main Parameters

Material	Silica	InP	Units
Thickness t	1.00	0.35	mm
Refractive index n	1.444	3.175	@ 1530 nm
Linear dispersion	-1.190×10^{-5}	-1.141×10^{-4}	nm^{-1}
Quadratic dispersion	-4.037×10^{-9}	$+2.788 \times 10^{-7}$	nm^{-2}
Optical thickness nt	1444	1111	μm
Front echo halfwidth	74.5	74.5	μm
Backecho displacement δz_2	+18.2	+61.1	μm
Backecho broadening parameter θ_2	-4.144×10^{-4}	$+1.002 \times 10^{-2}$	—

to affect the accuracy of the determination of the residual reflectance of the rear face if antireflective coated.

C. Antireflective Stack Phase Dispersion Effects

Let us now consider an antireflective stack deposited on the rear face of a plane silica window, 1 mm thick. The materials used in this antireflective stack are, respectively, silica for the low-index layers and tantalum pentoxide for the high-index layers. The deposition process is a dual ion beam sputtering technique (DIBS). The dispersion of the refractive index of the two types of layer can be described by the following relations:

$$\text{SiO}_2 \quad n_{\text{SiO}_2}(\lambda) = 1.48144 + \frac{0.007369}{\lambda^2}, \quad (29)$$

$$\text{Ta}_2\text{O}_5 \quad n_{\text{Ta}_2\text{O}_5}(\lambda) = 2.08527 + \frac{0.016975}{\lambda^2} + \frac{0.001625}{\lambda^4}, \quad (30)$$

where λ is in micrometers. For our simulations, we also considered two different antireflective stacks, the first one (hereafter called AR2) corresponding to the optimal two layer solutions [19] at one wavelength (here 1530 nm), and the second one (hereafter called AR4) to a possible solution for a broadband application (between 1510 and 1560 nm). The AR2 stack is described by the formula Silica/0.366H – 1.326L/Air, while the structure of the AR4 stack is Silica/1.980H – 0.967L – 1.579H – 0.718L/Air. Figures 4 and 5 show the variations with the wavelength of the reflectance and phase behavior of each stack.

If we consider only the spectral dispersion of the phase term and assume a constant value for the reflectance, the specific effect of this stack phase dispersion can be defined by using the following method. First, we have to compute the integral quantity $I(z)$,

$$I(z) = \frac{1}{\delta\lambda\sqrt{\pi}} \int_{\lambda} e^{-\left(\frac{\lambda-\lambda_0}{\delta\lambda}\right)^2} \cos\left[\varphi_{\text{AR}}(\lambda) + \frac{4\pi}{\lambda} z\right] d\lambda, \quad (31)$$

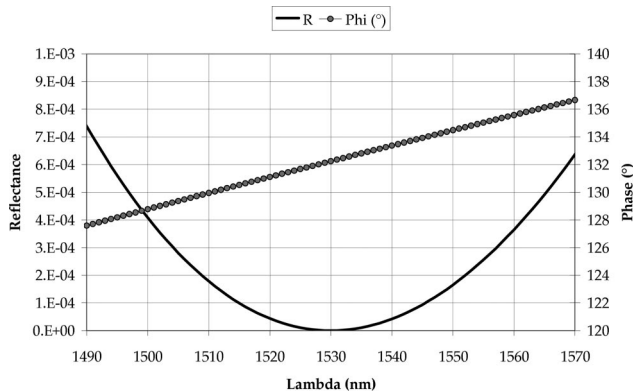


Fig. 4. Spectral properties of the AR2 stack.

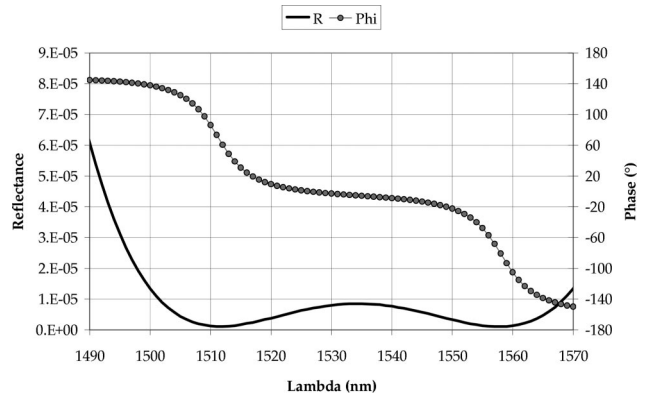


Fig. 5. Spectral properties of the AR4 stack.

where λ_0 is, as defined in Subsection 3.B, the central wavelength of the spectral profile of the source [see Eq. (8)], and $\delta\lambda$ its half-width at $1/e$. Then we have to extract from this first result the position and the value of the envelope maximum. It is in fact the same kind of approach as described in Subsection 3.C, except for using a numerical computation instead of an analytical one. In any case (AR2 or AR4), the displacement of the top of the echo is less than $2 \mu\text{m}$, while its maximum value remains equal to 1. The antireflective stack phase dispersion therefore has no impact on the accuracy of the reflectance measurement.

D. Spectral Averaging Effects

In this last theoretical section, we will consider only the effect of the variations of the stack reflectance on the wavelength on the accuracy of our OLCR measurement method. As described above, this effect can be estimated by numerically computing the following integral:

$$I(z) = \frac{\int_{\lambda} R(\lambda)P(\lambda)\cos\left[\frac{4\pi}{\lambda} z\right] d\lambda}{\int_{\lambda} P(\lambda)d\lambda}, \quad (32)$$

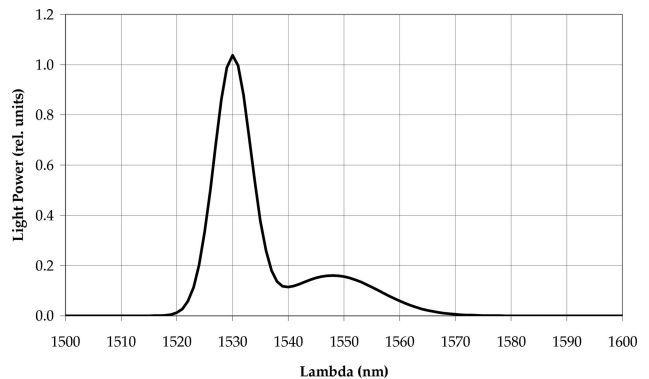


Fig. 6. Spectral profile of an EDFA-ASE source.

Table 2. Spectral Averaging Effects—Influence of the Source Profile

Antireflective Stack	AR2	AR4
Theoretical reflectance at 1530 nm	0	8.00×10^{-6}
Gaussian source 1 nm half-width	2.72×10^{-7}	7.97×10^{-6}
Gaussian source 5 nm half-width	5.42×10^{-6}	7.69×10^{-6}
Gaussian source 10 nm half-width	2.07×10^{-5}	6.92×10^{-6}
EDFA-ASE source	4.92×10^{-5}	6.69×10^{-6}

where $R(\lambda)$ is the stack reflectance and $P(\lambda)$ is the spectral profile of the source. We selected four different source profiles, i.e., three Gaussian profiles with various half-widths (1, 5, and 10 nm) and a more complex profile in accordance with the spectral distribution of an erbium doped fiber amplifier in amplified spontaneous emission (EDFA-ASE) regime. The shape of this last profile is shown in Fig. 6.

The results of this modeling are summarized in Table 2. It shows the variation of the measured reflectance with the spectral profile of the source for the two AR stacks defined in Subsection 3.C. All the Gaussian sources are centered at 1530 nm. For the single wavelength antireflective stack (AR2), the measurement error induced by the use of a 5 nm source half-width is about 5×10^{-6} , while for the broadband one (AR4) this error is lower and reaches only 3×10^{-7} . As expected, the best results are obtained by using the narrowest profile (1 nm half-width): this specific point is discussed in detail in Section 5.

Finally, we stress that the spectral variations of the reflectance can have a spectacular effect on the shape of the echo, as illustrated in Fig. 7 for the AR2 stack and the 5 nm half-width Gaussian source.

4. Experimental Results

A. Optical Setup

The optical setup used to achieve an experimental demonstration of this measurement method is identical to the schematic descriptions given in Figs. 1 (collimated configuration) and 3 (focused configuration). The light source is an EXFO (Quebec, Canada) FLS-2600A tunable laser used in the ASE mode [20]

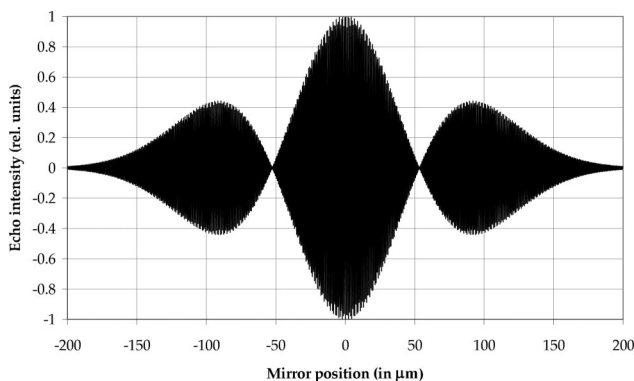


Fig. 7. Influence of the spectral variation of the reflectance on the echo shape.

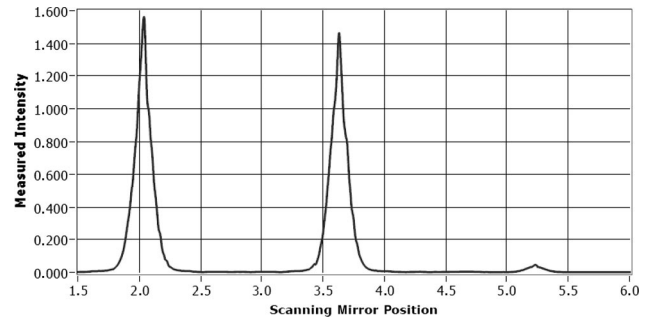


Fig. 8. Bare silica window, experimental LCOR recording.

and whose spectral profile is in accordance with the data in Fig. 6. The 3 dB coupler is manufactured with standard single mode fibers, Corning SMF-28 type (mode radius $5.25 \mu\text{m}$ at 1530 nm). The collimating lenses are identical in both arms and characterized by a focal length of 25.3 mm. The translation speed of the metallic mirror is equal to 1.8 mm/s and generates an intermediate frequency around 2.5 kHz. The current delivered by the InGaAs photodiode connected on the fourth arm of the 3 dB coupler is amplified by a variable-gain low-noise current amplifier (FEMTO, Berlin, Germany, DLPCA-200) [21] and digitized through a 16 bit 200 kS/s National Instruments (Austin, Texas) data acquisition card. The recorded data are numerically processed by using a synchronous detection scheme at the intermediate frequency, and then filtered by a low-pass filter with a cutoff frequency of about 250 Hz. Finally, to obtain an accurate evaluation of the ratio between the intensity of two echoes, we isolate in the filtered signal the part corresponding to the reference echo, and we compute numerically the result of the convolution of this reference signal with the recorded one: the ratio of the peaks corresponding to each echo provides the expected result.

B. Bare Silica Substrate

The first experimental test has been performed on a 1 mm thick bare silica window in a collimated configuration (see Fig. 1). The distance between the collimating lens and the front face of the window is equal to 220 mm. The shape of the filtered signal associated with a 6 mm length mirror scan is given in Fig. 8. As indicated in Section 2, the first echo is associated with the reflection on the front face of the silica window, the second one with the reflection on

Table 3. Bare Silica Window and Collimated Configuration; Comparison of Theoretical and Experimental Data

Echo Order	1	2	3
Theoretical reflectance	3.30×10^{-2}	3.09×10^{-2}	3.37×10^{-5}
Experimental reflectance	—	3.14×10^{-2}	3.44×10^{-5}
Absolute error	—	4.7×10^{-4}	6.7×10^{-7}
Relative error	—	1.4%	2.2%

Table 4. Bare Silica Window and Focused Configuration; Comparison of Theoretical and Experimental Data

Echo Order	1	2	3
M_k factor (theoretical)	1.0000	0.9455	0.0294
M_k factor	1.0000	0.9493	0.0293

its rear face, and the third one with the first multiple reflection into this window (reflection on the rear face, internal reflection on the front face, followed by a new reflection on the rear face).

In Table 3 we summarized the data connected with this collimated measurement configuration. As defined in Section 2, the theoretical value of the reflectance for the first echo is used to compute the calibrated data associated with the experimental reflectance of the final two echoes. The agreement is excellent and allows estimating the intrinsic accuracy of the method without the effect of any kind of spectral averaging (relative error around 2%).

The second experimental test corresponds again to a bare silica window, but this time with an OLCR setup implemented in a focused configuration. The distances between the extremity of the single mode fiber and the lens (28.7 mm) and between the lens and the front face of the windows (216.6 mm) are identical to the ones defined in the corresponding paragraphs of Subsection 3.A. The coupling efficiencies of the sample arm are then equal to the ones presented in this section, i.e., $\eta_1 = 100\%$; $\eta_2 = 95.6\%$; and $\eta_3 = 84.5\%$. To take into account this new situation, we decided to use the M_k factors [see Eq. (12)] instead of the R_k echoes reflectance to perform the comparison (Table 4) between experimental results and theoretical predictions. The agreement is again excellent (relative error less than 0.5%), which shows that the proposed theoretical modeling provides an accurate description of the single mode fiber coupling efficiency phenomena.

The final feature that can be extracted from this OLCR characterization of a bare silica window is the ultimate sensitivity of our experimental setup. Figure 9 is a zoomed view of the low part of the signal corresponding to Fig. 8. We can notice on this draw-

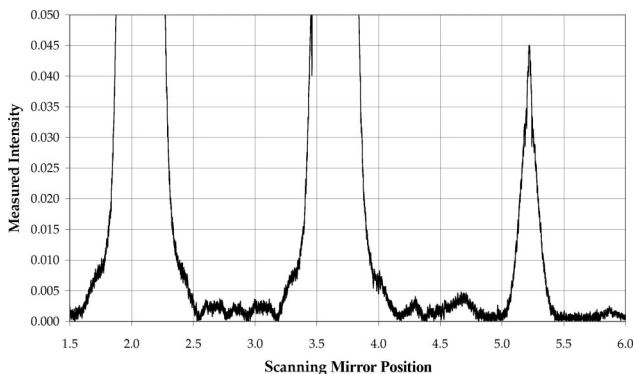


Fig. 9. Bare silica window, zoomed view of the OLCR recording.

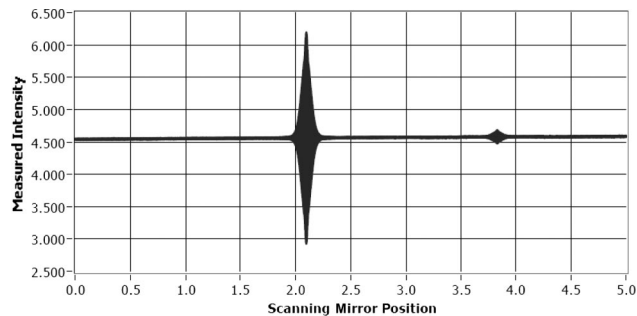


Fig. 10. AR-coated silica window, raw signal.

ing that the intensity of the third echo is recorded with a signal-to-noise ratio better than 10. Thanks to the coherent scheme used for echo detection, this ratio becomes equal to 100 for the reflectance coefficients, as defined by Eq. (12) or (13). It means that the lowest detectable reflectance is 100 times lower than the third recorded echo, i.e., about 5×10^{-7} .

C. AR-Coated Window Samples

Since the OLCR measurement method is completely qualified by the experimental results described in the previous section, we applied it to the characterization of coated samples. The first one is a silica window having one side coated with a broadband antireflective stack identical to the one called AR2 in Subsection 3.C. The raw and filtered signals recorded during a scan of the plane mirror are shown in Figs. 10 and 11 (OLCR focused configuration). Only two echoes can be obviously detected, the first one corresponding to the reflection on the uncoated front face and the second to the contribution of the AR-coated rear face.

To extract the reflectance coefficient R_{AR} of the coated face, we used Eq. (13), replacing the R_2 coefficient by the product of R_{AR} times the square of the transmission of the front face, i.e.,

$$R_2 = R_{AR}(1 - R)^2 = R \frac{\eta_1 \eta_M(z_1)}{\eta_2 \eta_M(z_2)} \times \left[\frac{S_2}{S_1} \right]^2, \quad (33)$$

where $R = (n - 1)/(n + 1)^2$ is the theoretical value of the reflectance coefficient of the bare silica at 1530 nm. Here we have $\eta_1 = \eta_M(z_1) = \eta_M(z_2) = 1$; $\eta_2 = 0.956$ (see Subsection 3.C); $R = 3.30 \times 10^{-2}$;

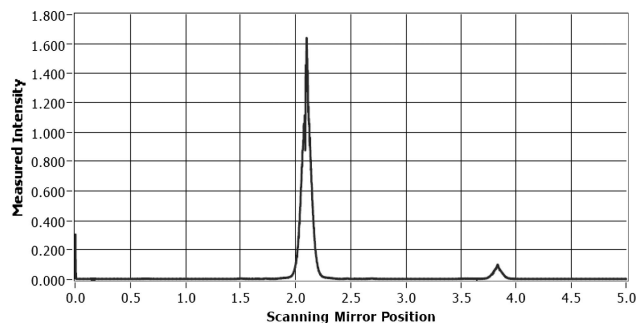


Fig. 11. AR-coated silica window, filtered signal.

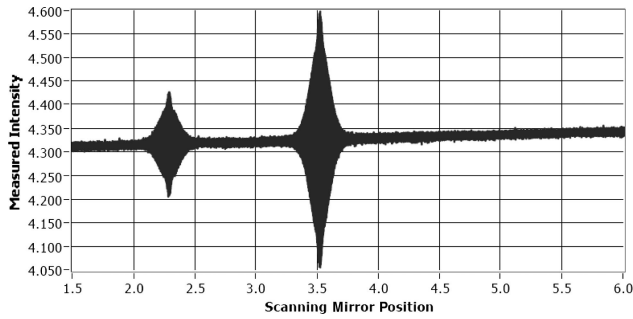


Fig. 12. AR-coated InP wafer, raw signal.

$S_2 = 0.1055$ a.u.; and $S_1 = 1.644$ a.u., which leads to $R_{AR} = 1.520 \times 10^{-4} \pm 4 \times 10^{-6}$.

This experimental result has to be compared to the theoretical computation presented in Table 2, at line EDFA-ASE Source, for the AR2 antireflective stack (i.e., 4.92×10^{-5}). The discrepancy between these two results reveals the impact of small manufacturing errors and shows that the accuracy of the OLCR method can be used to optimize the driving parameters of a deposition process.

The second coated sample is an InP wafer having its finely polished, first face, antireflective coated, while the second face is slightly ground. Therefore, it is impossible to place the uncoated face in front and to use it as a reference for calibration. The calibration has been achieved here by comparing the intensity of the echo to the one recorded when the sample is replaced by a reference metallic mirror (calibrated reflectance 92%). To qualify this alternative method, we have applied it to the previously studied silica sample, and the new determination falls within the uncertainty range of the first one. The raw and filtered signals recorded during a scan of the mirror are shown in Figs. 12 and 13 (OLCR focused configuration). As indicated previously, the first echo corresponds with the reflection on the coated front face while the second is associated with the scattering on the ground rear face. It explains why the ratio between the two echoes is so low despite the high value of the refractive index of the indium phosphide (about 3.7). After processing and applying the proposed alternative calibration procedure, we obtained a value of $2.80 \times 10^{-5} \pm 6 \times 10^{-6}$ for the reflectance coefficient of the InP coated face.

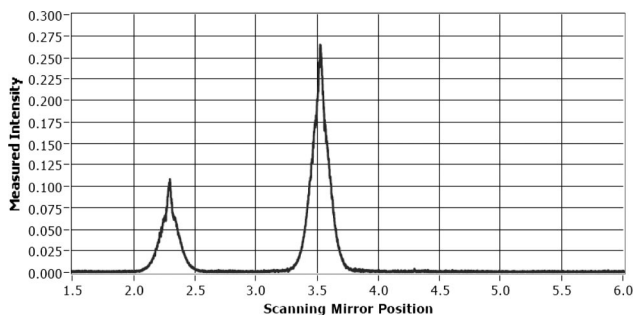


Fig. 13. AR-coated InP wafer, filtered signal.

5. Conclusions and Perspectives

We showed that OLCR is an efficient tool with which to achieve accurate characterization of the performances of antireflective optical coatings deposited on a plane window. The theoretical analysis that we performed has shown that the focused calibration is the most efficient method in terms of alignment and parallelism tolerances for the window. Moreover, the use of the computed coupling efficiencies in an open loop is a good way to improve the accuracy of this measurement scheme. We also showed that the refractive index dispersion of the window and the phase dispersion of the optical coating have no significant impact on the accuracy of the measurements.

Actually, the most critical parameter is the spectral bandwidth of the source. The use of a narrow-band source is a key point to avoid the echo broadening effect associated with the spectral dispersion of the refractive index of the window. Moreover, such a source also permits us to determine the reflectance coefficient at a given wavelength with negligible spectral averaging phenomena. But on the other hand, the spectral width of the source has to be large enough to ensure a perfect separation of the contributions of the backreflected signal from each face. This last condition can be described by the following expression:

$$\sqrt{R_1} \times e^{-\left(\frac{t}{\Delta z} [n_0 - \lambda_0 (\partial n / \partial \lambda)_{\lambda_0}]\right)^2} \leq 10^{-2} \times \sqrt{R_2}, \quad (34)$$

where Δz is the half-width of the echo at $1/e$. The minimal bandwidth of the source is indeed defined by the relation

$$\delta \lambda \geq \frac{\lambda_0^2 \times \sqrt{4 \ln(10) + \ln(R_1/R_2)}}{2\pi \sqrt{2t} [n_0 - \lambda_0 (\partial n / \partial \lambda)_{\lambda_0}]}. \quad (35)$$

For a 1 mm thick silica window and an expected resolution of about 10^{-7} on the reflectance measurement of the AR-coating performances, relation (35) leads a source whose minimal half-width at $1/e$ is about 1 nm. It means that a broadband source followed by a low performance monochromator can be used with the OLCR method. That way the value of the AR-coating reflectance at a specific wavelength can be determined with great accuracy. But such a source allows one to perform a measurement of the spectral dependence of this reflectance coefficient with a 1 nm resolution on a spectral range defined by the intrinsic features of the broadband source.

References

1. T. Bosselman and R. Ulrich, "High-accuracy position sensing with fiber-coupled white-light interferometers," in *Proceedings of the Second International Conference on Optical Fiber Sensors*, M. Nijhoff, ed. (Springer Verlag, 1984), pp. 361–364.
2. H. C. Lefevre, "White-light interferometry in optical fibre sensors," in *Proceedings of the 7th Optical Fiber Sensors Conference* (Institution of Radio and Electronics Engineering, Sydney, Australia, 1990), pp. 345–352.

3. M. Lequime, C. Lecot, H. Giovannini, and S. J. Huard, "Dual-wavelength passive homodyne detection unit for fiber-coupled white-light interferometers," in *Fiber Optic Sensors IV*, R. T. Kersten, ed., Proc. SPIE **1267**, 288–298 (1990).
4. P. Sansonetti, M. Lequime, D. Engrand, J. J. Guerin, R. Davidson, S. S. Roberts, B. Fomari, M. Martinelli, P. Escobar Rojo, V. Gusmeroli, P. Ferdinand, J. Plantey, M. F. Crowther, B. Culshaw, and W. C. Michie, "Intelligent composites containing measuring fiber-optic networks for continuous self-diagnosis," in *Fiber Optic Smart Structures and Skins IV*, R. O. Claus and E. Udd, eds., Proc. SPIE **1588**, 198–209 (1991).
5. K. Takada, A. Himeno, and K. Yukimatsu, "Phase-noise and shot-noise limited operations of low coherence optical time domain reflectometry," Appl. Phys. Lett. **59**, 2483–2485 (1991).
6. K. Kasaya, K. Yoshikuni, and H. Ishii, "Measurements of a semiconductor waveguide using a low-coherence interferometric reflectometer," IEEE Photon. Technol. Lett. **8**, 251–253 (1996).
7. E. A. Swanson, J. A. Izatt, M. R. Hee, D. Huang, C. Lin, J. S. Schuman, C. A. Puliafito, and J. G. Fujimoto, "In vivo retinal imaging by optical coherence tomography," Opt. Lett. **18**, 1864–1866 (1993).
8. G. J. Tearney, B. E. Bouma, S. A. Boppart, B. Golubovic, E. A. Swanson, and J. G. Fujimoto, "Rapid acquisition of in vivo biological images by use of optical coherence tomography," Opt. Lett. **21**, 1408–1410 (1996).
9. U. Morgner, W. Drexler, F. X. Kärtner, X. D. Li, C. Pitris, E. P. Ippen, and J. G. Fujimoto, "Spectroscopic optical coherence tomography," Opt. Lett. **25**, 111–113 (2000).
10. W. V. Sorin and D. F. Gray, "Simultaneous thickness and group index measurement using optical low-coherence reflectometry," IEEE Photon. Technol. Lett. **4**, 105–107 (1992).
11. M. Haruna, M. Ohmi, T. Mitsuyama, H. Tajiri, H. Maruyama, and M. Hashimoto, "Simultaneous measurement of the phase and group indices and the thickness of transparent plates by low-coherence interferometry," Opt. Lett. **23**, 966–968 (1998).
12. M. Duncan, J. Reintjes, and M. Bashkansky, "Subsurface defect detection in materials using optical coherence tomography," Opt. Express **2**, 540–545 (1998).
13. B. E. A. Saleh and M. C. Teich, *Fundamentals of Photonics* (Wiley-Interscience, 1991).
14. H. Kogelnik, "Coupling and conversion coefficients for optical modes," in *Microwave Research Institute Symposia Series*, J. Fox, ed. (Polytechnic Press, 1964), Vol. 14, p. 333.
15. M. Saruwatari and K. Nawata, "Semiconductor laser to single-mode fiber coupler," Appl. Opt. **18**, 1847–1856 (1979).
16. H. Giovannini, S. Huard, and M. Lequime, "Influence of chromatic dispersion on a dual-wavelength passive-homodyne detection method for fiber-coupled interferometers," Appl. Opt. **33**, 2721–2733 (1994).
17. M. J. Weber, *Handbook of Optical Materials* (CRC Press, 2003).
18. P. Martin, E. M. Skouri, L. Chusseau, C. Alibert and H. Bissessur, "Accurate refractive index measurements of doped and undoped InP by a grating coupling technique," Appl. Phys. Lett. **67**, 881–883 (1995).
19. H. A. Macleod, *Thin-Film Optical Filters*, 3rd ed. (Institute of Physics, 2001).
20. <http://www.exfo.com/en/products/ProductsFamily.asp?Family=201>.
21. http://www.femto.de/datasheet/DE-DLPCA-200_15.pdf.